Multiple flat bands and topological Hofstadter butterfly in twisted bilayer graphene close to the second magic angle

Xiaobo Lu[a,1,2], Biao Lian[b,1], Gaurav Chaudhary[c,1,3], Benjamin A. Piot[d], Giulio Romagnoli[e], Kenji Watanabe (渡邊賢司)[f], Takashi Taniguchi[f], Martino Poggio[e], Allan H. MacDonald[c,2], B. Andrei Bernevig[g], and Dmitri K. Efetov[a,2]

[a]Institut de Ciencies Fotoniques, The Barcelona Institute of Science and Technology, Barcelona 08860, Spain; [b]Princeton Center for Theoretical Science, Princeton University, Princeton, NJ 08544; [c]Department of Physics, The University of Texas at Austin, Austin, TX 78712; [d]Laboratoire National des Champs Magnétiques Intenses, Université Grenoble Alpes, 38000 Grenoble, France; [e]Department of Physics, University of Basel, Basel 4056, Switzerland; [f]National Institute for Materials Science, Tsukuba 305-0044, Japan; and [g]Department of Physics, Princeton University, Princeton, NJ 08544

Moiré superlattices in two-dimensional van der Waals heterostructures provide an efficient way to engineer electron band properties. The recent discovery of exotic quantum phases and their interplay in twisted bilayer graphene (tBLG) has made this moiré system one of the most renowned condensed matter platforms. So far studies of tBLG have been mostly focused on the lowest two flat moiré bands at the first magic angle $\theta_{m1} \sim 1.1°$, leaving high-order moiré bands and magic angles largely unexplored. Here we report an observation of multiple well-isolated flat moiré bands in tBLG close to the second magic angle $\theta_{m2} \sim 0.5°$, which cannot be explained without considering electron–election interactions. With high magnetic field magnetotransport measurements we further reveal an energetically unbound Hofstadter butterfly spectrum in which continuously extended quantized Landau level gaps cross all trivial band gaps. The connected Hofstadter butterfly strongly evidences the topologically nontrivial textures of the multiple moiré bands. Overall, our work provides a perspective for understanding the quantum phases in tBLG and the fractal Hofstadter spectra of multiple topological bands.

moiré | two-dimensional | nanoelectronics | van der Waals | materials

Twisted bilayer graphene (tBLG) has emerged as a rich platform to study strong correlations (1), superconductivity (2–8), magnetism (9), and band topology (10). Stacking two graphene sheets with a slight rotation by an angle θ creates a moiré superpotential. The renormalized bands have C_{6z}, C_{2x} rotational symmetries and time-reversal symmetry T. This leads to decoupled valleys (11) and the formation of a mini moiré Brillouin zone (Fig. 1A) with two Dirac cones with identical helicity (Fig. 1B), which makes the resulting two lowest moiré bands at each valley topologically different from the two π bands in monolayer graphene in which the total helicity vanishes. They carry a nonzero Dirac helicity $\eta = \pm 2$ (Fig. 1B), which is protected by C_{2z}T symmetry. These attributes prohibit the construction of local symmetric Wannier functions and define the nontrivial topology of tBLG (12–15).

The magic angles in tBLG are a series of well-defined twist angles for which the moiré bands are predicted to become ultraflat (11). While the tBLG at $\theta_{m1} \sim 1.1°$ is already extensively studied, tBLG at well-defined smaller magic angles (i.e., $\theta_{m2} \sim 0.5°$), in which inhomogeneity of moiré patterns is much more sensitive to twist-angle fluctuations (16), has so far rarely been experimentally investigated. Since tBLG at θ_{m2} offers an exceedingly large moiré unit cell, it gives rise to a multitude of closely packed flat moiré bands. Crucially, the moiré wavelength for tBLG at θ_{m2} of $\lambda \sim 30$ nm is much larger than for θ_{m1} tBLG or for graphene/hexagonal boron nitride (hBN) moiré superlattices, and hence inducing one magnetic flux per unit cell, required to obtain a Hofstadter butterfly, can be easily achieved at

much lower fields (approximately six times) (17–19). Together these characteristics make tBLG at θ_{m2} an ideal platform to explore multiple moiré bands and their Hofstadter butterfly spectra which are rendered with interactions and novel band topology.

Results

In this article we present magnetotransport measurements of tBLG devices, with θ close to the predicted second magic angle $\theta_{m2} \sim 0.5°$. Our tBLG device is encapsulated with crystallographically nonaligned insulating layers of hBN and its carrier concentration n is capacitively controlled by an underlying graphite layer (Fig. 1D) and calibrated with quantum oscillations in out-of-plane magnetic field $B_\perp$ (*SI Appendix*). Fig. 1 F and G show the evolution of the longitudinal resistance R_{xx} and the Hall density n_H as a function of n. R_{xx} exhibits peaks and n_H sign changes at equally spaced, integer multiples of n_s, $n = sn_s$, and marks the transitions between the individual bands. (We attribute the Hall density sign changes at noninteger multiples of n_s that are not accompanied by resistance maxima to van Hove singularities within the bands.) The resistance peaks are strongly enhanced by a small $B_\perp$-field (Fig. 1E) and develop thermally activated, gapped behavior (*SI Appendix*, Figs. S2–S4) but are

---

Significance

Multiple flat bands in high-quality twisted bilayer graphene close to the theoretically predicted second magic angle are observed. These well-isolated flat moiré bands host a nontrivial topology which is evidenced by a connecting multiband Hofstadter butterfly spectrum. This work provides a perspective for understanding the emergent quantum phases (i.e., strong correlation and band topology) in twisted bilayer graphene and the fractal Hofstadter spectra of multiple topological bands.
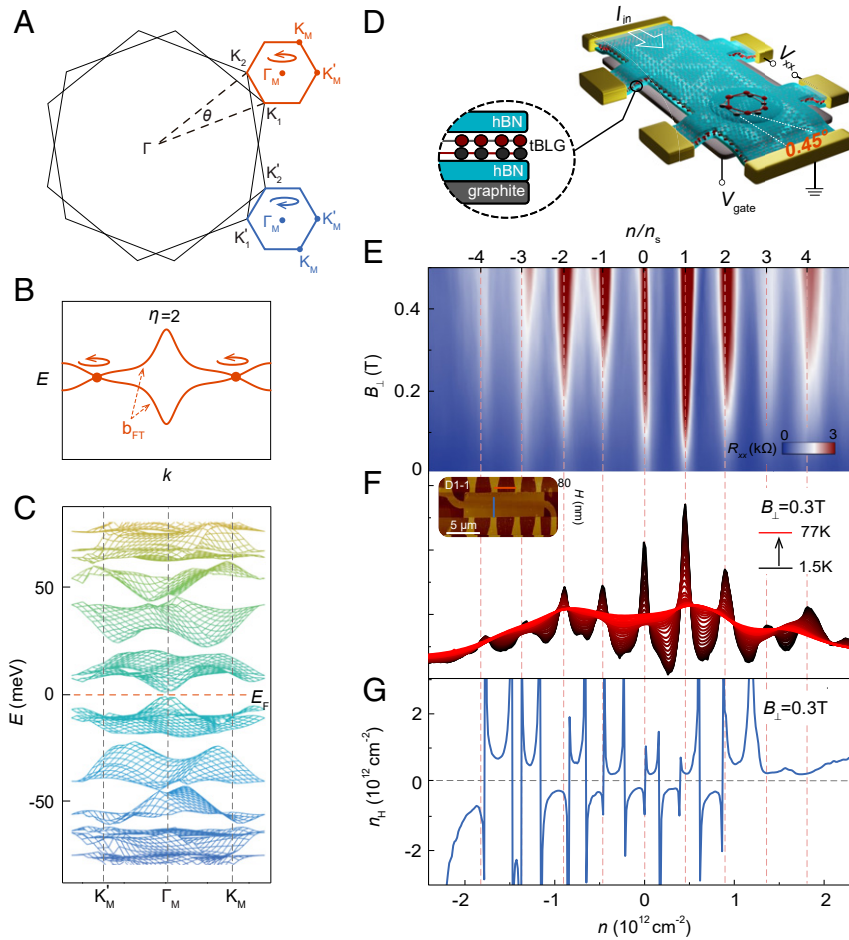

PHYSICS

Fig. 1. Multiple moiré bands with nonzero helicity in $\theta = 0.45°$ tBLG. (A) Mini moiré Brillouin zones are defined by two Dirac cones with a total Dirac helicity $\eta = \pm 2$. (B) Nonzero total Dirac helicity in the lowest two moiré bands inside of one valley. (C) Hartree–Fock band structure calculations of 0.45° tBLG with Coulomb interaction show multiple moiré bands, which are separated at the Fermi energy E_F. Here the high symmetry points of the Brillouin zone are K_M and Γ_M. (D) Schematic of the hBN encapsulated $\theta = 0.45°$ tBLG device with a graphite bottom gate. (E) Color plot of the longitudinal resistance R_{xx} vs. carrier density n and out-of-plane magnetic field $B_\perp$ ($T = 1.5$ K). (F) R_{xx} vs. n at different temperatures and $B_\perp = 300$ mT. (Inset) The atomic force microscopy image of a typical tBLG device. (G) Hall carrier density $n_H = -B_\perp/(eR_{xy})$ as a function of gate-induced carrier density n measured at $B_\perp = 300$ mT and $T = 1.5$ K.

insensitive to parallel B-field (*SI Appendix*, Fig. S5). This suggests an orbital origin and agrees with the fact that small $B_\perp$-fields can gap out the $C_{2z}T$ protected Dirac nodes or increase a small band gap.

The noninteracting band structure of tBLG around θ_{m2} contains eight strongly convoluted 4-fold spin-valley degenerate low-energy flat bands (*SI Appendix*, Fig. S10B). To account for interaction effects in the flat bands, we perform Hartree–Fock calculations including Coulomb interactions with random seeds, which allow for spontaneous symmetry breaking (*SI Appendix*, section 5). These show that Coulomb interactions spontaneously break C_{3z}, while preserving the $C_{2z}T$ symmetry. As a direct consequence, the moiré bands separate above and below the Fermi energy E_F and become almost nonoverlapping except for point-like connections.

This is seen in Fig. 1C (for E_F at the charge neutrality point [CNP], $s = 0$) and in *SI Appendix*, Fig. S10A (for E_F at integer band fillings $s = 1, 2, 3, 4$), which show the Hartree–Fock moiré bands in one valley of $\theta = 0.45°$ tBLG. Here, each separate band remains 4-fold degenerate and can intake $n_s = 4/\Omega_m$ carriers, where Ω_m is the area of the moiré unit cell. The carrier density can be expressed by integer multiples of band fillings sn_s, which define the integer band filling factor $s \in \mathbb{Z}$. For $s = 0, \pm 1, \pm 3, \pm 4$, the band structure is semimetallic with two Dirac points per spin per valley at E_F, while for filling $s = \pm 2$ a small indirect gap occurs. In particular, we find that the helical Dirac nodes at the CNP, which

are responsible for the nontrivial topology, are quite robust for both interacting and noninteracting calculations, although they may deviate from high symmetry points due to C_{3z} symmetry breaking.

We compare the Hartree–Fock spectrum with transport measurements of a tBLG device with $\theta \sim 0.45°$ and find good agreement with its nonoverlapping bands picture. The experimentally resolved peaks in R_{xx} (equally spaced at $n = sn_s$) and the sharp interband transitions in n_H indicate that the bands are nonoverlapping, either semimetallic or separated by small gaps (*SI Appendix*, Fig. S2A), in good agreement with the Hartree–Fock calculations. Since the studied devices have θ close to the predicted second magic angle $\theta_{m2} \sim 0.5°$, these findings support the existence of flat bands and strong electronic interactions. However, we do not yet observe correlation-driven insulating states as in the case of tBLG at θ_{m1}. This may be due to suppression of the on-site Coulomb energy for a larger moiré wavelength (~ 10 meV for dielectric constant $\epsilon \sim 5$), the larger noninteracting bandwidths (~ 10 meV), and the close energetic proximity of the flat bands.

When the $B_\perp$-field is increased further (Fig. 2A), Landau levels (LL) develop within the individual bands and form gaps with nonzero Chern numbers ($C = 4, 8, 12, \ldots$ due to spin/valley degeneracy), which manifest themselves as dips in R_{xx} (blue). These dips trace back to the band edges at integer fillings $n/n_s = s$ at zero $B_\perp = 0$ T and follow a well-defined slope $dn/dB_\perp = Ce/h$ in
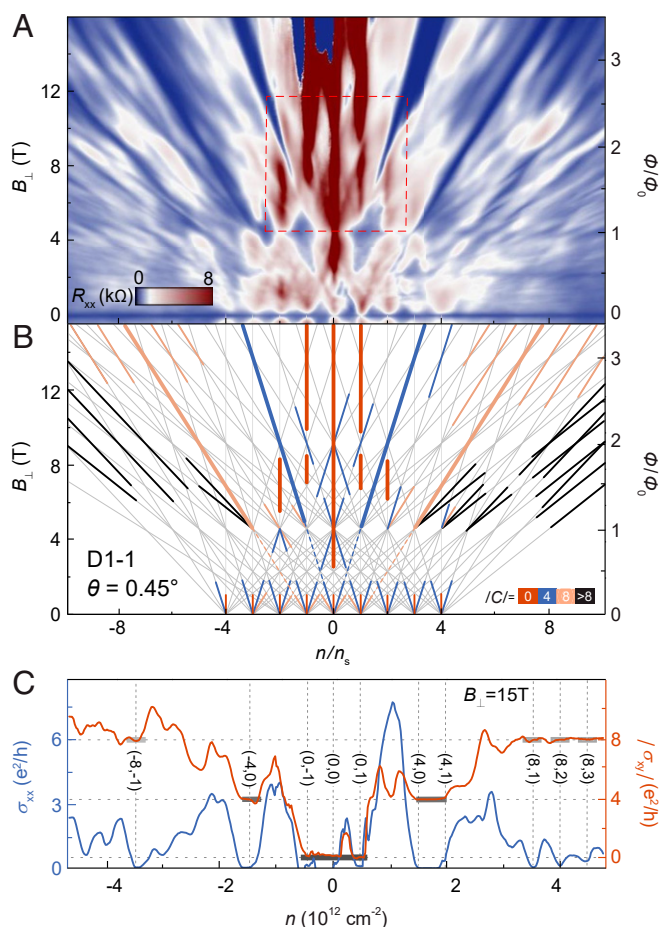
Fig. 2. Unbounded and connected Hofstadter butterfly spectrum. (A) Hofstadter spectrum of the $\theta = 0.45°$ tBLG device, revealed by the color plot of R_{xx} vs. carrier density n and $B_\perp$. (B) Schematic identifying visible LL gaps from A. Vertical solid lines indicate single-particle band gaps $(0, s)$ between the moiré bands, and diagonal solid lines indicate Hofstadter LL gaps (C, s), which emerge from the band edges. (C) Longitudinal conductance σ_{xx} and Hall conductance $|\sigma_{xy}|$ vs. n, measured at $B_\perp = 15$ T, show robust quantum Hall states with a nonmonotonic evolution with n, as expected from the Diophantine relation.

the n-$B_\perp$ phase space, where e is the electron charge and h is Planck's constant. Above $B_\perp > 8$ T robust quantum Hall states develop, with $R_{xx} \sim 0$ Ω, and with quantized plateaus in the Hall resistance of $R_{xy} \sim h/Ce^2$ (Fig. 2C). In contrast, all trivial band gaps have $C = 0$ and emerge from $B_\perp = 0$ T without a slope in $dn/dB_\perp = 0$. These gaps are identified by R_{xx} peaks (red) that follow straight vertical lines in the n-$B_\perp$ phase space. For clarity, we highlight the most pronounced gaps from Fig. 2A in Fig. 2B.

These findings indicate the formation of a fractal Hofstadter spectrum. The trajectories of the trivial band gaps and the topological LL gaps have a dense set of intersections at which only one of the gaps survives. The intersections occur at well-defined magnetic fields $B_\perp \sim 2.25$ T ($\phi \sim \phi_0/2$), $B_\perp \sim 4.5$ T ($\phi \sim \phi_0$), and $B_\perp \sim 9$ T ($\phi \sim 2\phi_0$), where $\phi = B_\perp \Omega_m$ is the magnetic flux per moiré unit cell and $\phi_0 = h/e$ is the magnetic flux quantum. The LL gaps in the n-$B_\perp$ diagram occur along lines that are described by the Diophantine relation, $n/n_s = C\phi/4\phi_0 + s$. This is further confirmed by R_{xy} versus n measurements in the quantum Hall regime at $B_\perp = 15$ T (Fig. 2C), which show a nonmonotonic evolution of the plateaus, consistent with the development of Hofstadter gaps within different moiré bands.

We denote the features of the Hofstadter gaps by (C, s), which have Chern number C and emerge from the band edges at filling $n = sn_s$. The fan diagram is dominated by a series of zero-field single-particle band gaps $(0, s)$ and by Hofstadter gaps $(\pm 4, s)$, $(\pm 8, s)$, which are strikingly not confined within the moiré band from which they emerge (at $B_\perp = 0$) but continuously extend into the higher-lying moiré bands at high $B_\perp$ and cross all $(0, s)$ band gaps. For example, the $(\pm 4, 0)$ gaps that are emerging from the CNP (blue diagonal lines) extend indomitably through several higher moiré bands, interrupting all band gaps $(0, s)$ at carrier densities $n = \pm sn_s$ (red vertical lines). The observed Hofstadter spectrum is qualitatively distinct from that of topologically trivial bands.

We highlight the differences by comparing typical Hofstadter spectra of topologically trivial and nontrivial bands (Fig. 3 A and B). For separated topologically trivial bands, the Hofstadter spectrum is confined within the energy bandwidth of each band. As $B_\perp$ increases, LLs from the band top and band bottom move toward the middle of the band and are annihilated around its center. This evolution of LLs in $B_\perp$ field defines an energetically bounded Hofstadter butterfly, where the LL spectra in one band are not connected to those of other bands (while one can devise trivial band structures with a connected spectrum, they are not generic). This is in stark contrast to the Hofstadter butterfly which is formed from topologically nontrivial bands (Fig. 3B). In all generality, the Hofstadter spectrum of a topological band is not energetically confined to the bandwidth of the band and can propagate until it connects to the Hofstadter spectrum of another band, which trivializes the total band topology (14, 20).

Such a topologically nontrivial, unbound, and connected Hofstadter butterfly spectrum is clearly present in the demonstrated $\theta = 0.45°$ tBLG device, as well as in several other devices with $\theta = 0.3°$ to $0.5°$ (SI Appendix, section 3). Fig. 3C displays a zoom-in of the dashed region in Fig. 2A and highlights the interplay between the trivial band gaps $(0, s)$ (red) and the Hofstadter gaps $(\pm 4, 0)$ (blue), where $(0, \pm 2)$ are clearly interrupted by $(\pm 4, 0)$ at $B_\perp \sim 9$ T ($\phi/\phi_0 = 2$). Similarly $(0, \pm 1)$ are interrupted by $(\pm 4, 0)$ at $B_\perp \sim 4.5$ T ($\phi/\phi_0 = 1$). These interruptions indicate the closing of the $(0, \pm s)$ band gaps between two neighboring bands, when their fillings coincide with that of the $(\pm 4, 0)$ LL gaps. This connects the Hofstadter spectra of the lowest two moiré bands with the spectra of all higher moiré bands, which is direct evidence of the nontrivial topology of tBLG and is in agreement with the theoretical predictions in refs. 14 and 20.

The experimentally obtained unbounded and connected Hofstadter spectrum is in good agreement with the theoretically calculated Hofstadter spectrum for low n ($|n/n_s| < 3$) (Fig. 3D and SI Appendix, Fig. S12B). It is calculated with a tBLG continuum model at $\theta = 0.45°$, which includes broken C_{3z} symmetry due to strain or Hartree–Fock mean fields (SI Appendix, section 6), to realistically mimic a strain-reconstructed tBLG device. We note that C_{3z} breaking could also be induced by angle disorders, which is however difficult to model and will not be discussed here (21). We find that the calculated $(\pm 4, 0)$ gaps continuously extend to the higher bands as expected. Moreover, experimentally we observe reemerged $(0,0)$ and $(0, \pm 1)$ gaps at $\phi > \phi_0$ and $(0, \pm 2)$ gaps in the range $\phi_0 < \phi < 2\phi_0$, which match the calculations only if C_{3z} breaking is considered (SI Appendix, Fig. S12). However, the observed Hofstadter spectra at high doping densities ($|n/n_s| > 3$) show deviations from the theoretical calculations. Theoretical calculations predict a series of $(4, s)$ and $(-4, -s)$ gaps ($s = 1, 2, 3, \ldots$) at $\phi > \phi_0$ in addition to the $(\pm 4, 0)$ gaps, while experimentally this region is dominated by the $(8, 1)$ and $(-8, -1)$ gaps, and only a $(4, 1)$ gap occurs at $\phi > 3\phi_0$. This discrepancy may have its origins in the nonnegligible role of interactions in the flat bands, which may considerably affect the Hofstadter spectrum of tBLG at large doping densities. In SI Appendix,
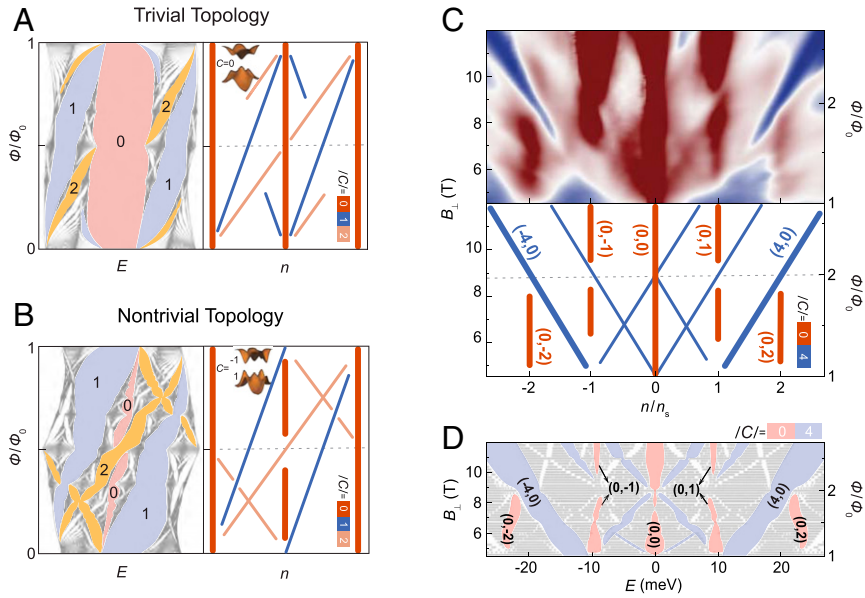
Lu et al.
Multiple flat bands and topological Hofstadter butterfly in twisted bilayer graphene close to the second magic angle

PNAS | 3 of 5
https://doi.org/10.1073/pnas.2100006118

PHYSICS

Fig. 3. Hofstadter butterfly with nontrivial topology. (*A* and *B*) Examples of Hofstadter spectra (*Left*) and corresponding gap schematics (*Right*) of two topologically trivial (*A*) and nontrivial $C = \pm1$ (*B*) bands. The topological Hofstadter spectrum shows distinct features, as its bands are connected at $\phi/\phi_0 = 1$, and the $C = 0$ band gaps are closed. Both *A* and *B* are calculated for tight-binding models (see *SI Appendix*, section 9). (*C*) Zoom-in on the Hofstadter spectrum in Fig. 2 *A* and *B*. The (±4, 0) LL gaps continuously extend into the higher-lying moiré bands and interrupt the (0, ±1) and (0, ±2) band gaps, showing the main signatures of the topological Hofstadter spectrum. (*D*) Calculated Hofstadter spectrum of $\theta = 0.45°$ tBLG shows good agreement with experiment (*C*).

section 6 we show that the inclusion of an electron-doping-induced Hartree term in the Hofstadter spectrum calculation suppresses the $(4, s)$ gaps, which suggests that interactions may be responsible for their experimental absence.

Discussion

One possible origin of the nontrivial unbound Hofstadter butterfly is the single-particle fragile topology hosted by the lowest two moiré bands of each spin and valley in tBLG (theoretically predicted and characterized by the $C_{2z}T$-protected nonzero Dirac helicity $\eta = \pm2$ at the CNP) (12–14). This fragile topology is further enhanced into a stable topology if the particle–hole symmetry of tBLG is preserved, which is robust against adding trivial particle–hole symmetric pairs of bands (15). It is theoretically shown that the Hofstadter spectrum of the lowest two topological moiré bands of tBLG is always connected with the spectrum of the higher moiré bands at sufficiently strong magnetic fields (up to infinity) (14) [although not universally protected by $C_{2z}T$ (20); see *SI Appendix*, section 4]. For a wide range of twist angles (including those studied in this paper), the $(\pm4,0)$ LL gaps are predicted to extend from the lowest two moiré bands to all the higher bands, forcing their Hofstadter spectra to be connected at $\phi/\phi_0 = 1$ (14). Accordingly, the band gap between two bands with connected Hofstadter spectra will close when the connection happens. We note that the flat moiré bands in tBLG can also develop correlated states of different stable topologies breaking $C_{2z}T$, for instance Chern insulators at the first magic angle, which are driven by interactions and stabilized by finite magnetic fields (22–27). At this point our results cannot radically rule out the possibility that either type of topology, $C_{2z}T$-preserved fragile topology or $C_{2z}T$-broken stable topology, is responsible for the connected Hofstadter spectra. The absence of correlated states in our experiment and the unbroken $C_{2z}T$ symmetry in our Hartree–Fock calculations, however, suggest the former is more likely.

In summary, we have reported a systematic magnetotransport study of tBLG close to θ_{m2}. Our results show 1) multiple well-isolated flat moiré bands in tBLG at θ_{m2}, which cannot be explained without considering interactions, 2) that tBLG is a highly tunable platform to study the Hofstadter butterfly, where the band topology can manifest itself qualitatively (trivial or nontrivial), and 3) that interaction effects play a clear role in tBLG Hofstadter spectra that merits further exploration.

Materials and Methods

Device Fabrication. The hBN/tBLG/hBN/graphite stacks were exfoliated and assembled using a van der Waals assembly technique. Monolayer graphene, thin graphite, and hBN flakes (~10 nm thick) were first exfoliated on an SiO₂ (~300 nm)/Si substrate, followed by the "tear and stack" technique with a polycarbonate/polydimethylsiloxane stamp to obtain the final hBN/tBLG/ hBN/graphite stack. The separated graphene pieces were rotated manually by the twist angle ~1°. We purposefully chose a larger twist angle during the heterostructure assembly due to the high risk of relaxation of the twist angle to the random lower values. To increase the structural homogeneity, we further carried out a mechanical cleaning process to squeeze the trapped blister out and release the local strain. We did not perform subsequent high-temperature annealing to avoid twist-angle relaxation. We further patterned the stacks with polymethyl methacrylate resist and CHF₃+O₂ plasma and exposed the edges of graphene, which was subsequently contacted by Cr/Au (5/50 nm) metal leads using electron-beam evaporation (Cr) and thermal evaporation (Au).

Measurement. Transport measurements were carried out in a refrigerator with a base temperature of 1.3 K and up to 16-T magnetic field. All the data without specific notification was measured at the base temperature. Standard low-frequency lock-in techniques were used to measure the resistance R_{xx} and R_{xy} with an excitation current of ~10 nA at a frequency of 19.111 Hz. A global gate voltage (+20 V) through Si/SiO₂ (~300 nm) is applied to reduce the contact resistance by tuning the charge carrier density separately in the device leads.

Twist Angle Extraction. The twist angle θ is deduced from the area of the moiré unit Ω_m given by $\Omega_m = \sqrt{3}a^2/4(1 - \cos\theta)$, where a is the lattice constant of graphene. Ω_m is extracted with two independent methods.

Method 1: Gate-induced carrier density is first calibrated with LLs. The carrier density of LL fanning out from CNP with total Chern number C strictly follows $n = CeB/h$. Here we use LL with index $C = 8$ to calibrate the carrier density. The area of moiré superlattice $\Omega_m = 4/n_s$, where n_s is the carrier density of a completely filled moiré band.

Lu et al.
Multiple flat bands and topological Hofstadter butterfly in twisted bilayer graphene close
to the second magic angle

Method 2: The Hofstadter butterfly is also used to extract Ω_m. When the magnetic flux per moiré unit cell given by $\phi = B\Omega_m$ equals to the magnetic flux quantum $\phi_0 = h/e$ (h, Planck's constant; e, magnitude of the electron charge), the Hofstadter spectrum will exhibit fractal signature (i.e., $B \sim 2.25$ T, $B \sim 4.5$ T, and $B \sim 9$ T corresponding to $\phi = \phi_0/2$, $\phi = \phi_0$, and $\phi = 2\phi_0$, respectively). The moiré area Ω_m can be described by $\Omega_m = \phi_0/B_0$ (B_0 is the magnetic field corresponding to $\phi = \phi_0$) where the straight lines of LL gaps in the n-B plot cross each other at integer band fillings.

Data Availability. All study data are included in the article and/or *SI Appendix*.

1. Y. Cao *et al.*, Correlated insulator behaviour at half-filling in magic-angle graphene superlattices. *Nature* **556**, 80–84 (2018).
2. Y. Cao *et al.*, Unconventional superconductivity in magic-angle graphene superlattices. *Nature* **556**, 43–50 (2018).
3. M. Yankowitz *et al.*, Tuning superconductivity in twisted bilayer graphene. *Science* **363**, 1059–1064 (2019).
4. X. Lu *et al.*, Superconductors, orbital magnets and correlated states in magic-angle bilayer graphene. *Nature* **574**, 653–657 (2019).
5. P. Stepanov *et al.*, Untying the insulating and superconducting orders in magic-angle graphene. *Nature* **583**, 375–378 (2020).
6. E. Codecido *et al.*, Correlated insulating and superconducting states in twisted bilayer graphene below the magic angle. *Sci. Adv.* **5**, eaaw9770 (2019).
7. H. S. Arora *et al.*, Superconductivity in metallic twisted bilayer graphene stabilized by WSe₂. *Nature* **583**, 379–384 (2020).
8. Y. Saito *et al.*, Independent superconductors and correlated insulators in twisted bilayer graphene. *Nat. Phys.* **16**, 926–930 (2020).
9. A. L. Sharpe *et al.*, Emergent ferromagnetism near three-quarters filling in twisted bilayer graphene. *Science* **365**, 605–608 (2019).
10. M. Serlin *et al.*, Intrinsic quantized anomalous Hall effect in a moiré heterostructure. *Science* **903**, eaay5533 (2019).
11. R. Bistritzer, A. H. MacDonald, Moire bands in twisted double-layer graphene. *Proc. Natl. Acad. Sci. U.S.A.* **108**, 12233–12237 (2011).
12. H. C. Po, H. Watanabe, A. Vishwanath, Fragile topology and Wannier obstructions. *Phys. Rev. Lett.* **121**, 126402 (2018).
13. Z. Song *et al.*, All "magic angles" are "stable" topological. *Phys. Rev. Lett.* **123**, 36401 (2019).
14. B. Lian, F. Xie, B. A. Bernevig, Landau level of fragile topology. *Phys. Rev. B* **102**, 1–7 (2020).
15. Z. Song, B. Lian, N. Regnault, A. B. Bernevig, Twisted bilayer graphene. II. Stable symmetry anomaly. *Phys. Rev. B* **103**, 205412 (2021).
16. H. Yoo *et al.*, Atomic and electronic reconstruction at the van der Waals interface in twisted bilayer graphene. *Nat. Mater.* **18**, 448–453 (2019).
17. C. R. Dean *et al.*, Hofstadter's butterfly and the fractal quantum Hall effect in moiré superlattices. *Nature* **497**, 598–602 (2013).
18. B. Hunt *et al.*, Massive Dirac fermions and Hofstadter butterfly in a van der Waals heterostructure. *Science* **340**, 1427–1430 (2013).
19. L. A. Ponomarenko *et al.*, Cloning of Dirac fermions in graphene superlattices. *Nature* **497**, 594–597 (2013).
20. J. Herzog-Arbeitman, Z. D. Song, N. Regnault, B. A. Bernevig, Hofstadter topology: noncrystalline topological materials at high flux. *Phys. Rev. Lett.* **125**, 236804 (2020).
21. A. Uri *et al.*, Mapping the twist-angle disorder and Landau levels in magic-angle graphene. *Nature* **581**, 47–52 (2020).
22. J. Liu, J. Liu, X. Dai, Pseudo Landau level representation of twisted bilayer graphene: Band topology and implications on the correlated insulating phase. *Phys. Rev. B* **99**, 1–9 (2019).
23. K. P. Nuckolls *et al.*, Strongly correlated Chern insulators in magic-angle twisted bilayer graphene. *Nature* **588**, 610–615 (2020).
24. I. Das *et al.*, Symmetry broken Chern insulators and Rashba-like Landau level crossings in magic-angle bilayer graphene. *Nat. Phys.*, 10.1038/s41567-021-01186-3. (2021).
25. S. Wu, Z. Zhang, K. Watanabe, T. Taniguchi, E. Y. Andrei, Chern insulators, van Hove singularities and topological flat bands in magic-angle twisted bilayer graphene. *Nat. Mater.* **20**, 488–494 (2021).
26. Y. Saito *et al.*, H Hofstadter subband ferromagnetism and symmetry broken Chern insulators in twisted bilayer graphene. *Nat. Phys.*, 10.1038/s41567-020-01129-4 (2021).
27. B. Lian *et al.*, Twisted bilayer graphene. IV. Exact insulator ground states and phase diagram. *Phys. Rev. B* **103**, 205414 (2021).

Lu et al.
Multiple flat bands and topological Hofstadter butterfly in twisted bilayer graphene close to the second magic angle

PNAS | 5 of 5
https://doi.org/10.1073/pnas.2100006118